Research Article

Microstructural peculiarities and textural characteristics of Ni–W sheet alloy after accumulative roll-bonding and annealing

Siham Koriche[1] · Saadia Boudekhani-Abbas[1] · Hiba Azzeddine[2] · Thierry Baudin[3] · Anne-Laure Helbert[3] · François Brisset[3] · Yanick Ateba Betanda[4] · Thierry Waeckerlé[4] · Djamel Bradai[1]

Abstract

In the present study, the through thickness morphological and textural characteristics of a Ni–14W sheet, processed by accumulative roll-bonding (ARB) up to 4 cycles ($\varepsilon = 3.2$) and annealed at 1100 °C for 1 h, were investigated using electron backscatter diffraction. In the internal layers, the microstructure exhibited a small grains size free of twins and contained high fraction of low angle grain boundaries due the domination of {001}⟨100⟩ Cube orientation. At the surface layers, grains were coarser and contained high fraction of twins, while texture was characterized by retained shear components. The results showed that the heterogeneity of annealed microstructure texture decreased with the increasing number of ARB processing. Particle stimulated nucleation mechanism was evidenced at the vicinity of some bonding interfaces due to the presence of metallic inclusions resulting from wire-brushing procedure. As a result, the orientation of the new recrystallized grains was rather random and the grain size was stabilized by a pining effect which contributed to the microstructure heterogeneity. A successful bonding was achieved with increasing number of ARB cycles as shown by the transformation of interfaces into grain boundaries and their subsequent migration.

Keywords Ni–W alloy · ARB · Microstructure · Recrystallization · {001}⟨100⟩ Cube texture

1 Introduction

Recently, Nickel (Ni) and its alloys have increasingly attracted scientific investigations due to their potential applications as coated conductor substrates for photovoltaic purposes [1]. In particular, Ni–W alloy is the most used material for Rolling Assisted Biaxially Textured Substrates (RABITS™) technique including severe cold rolling and annealing [2].The central challenge in developing such materials is to achieve special sharp {001}⟨100⟩ Cube texture (> 90% within 5° dispersion), temperature stability, low lattice constant misfit and mechanical strength [1]. In fact, {001}⟨100⟩ Cube texture is essential for subsequent epitaxial growth of the buffer and/or high temperature superconducting (HTS) materials such as Yttrium Barium Copper Oxide (YBCO) layers [1].The sharp {001}⟨100⟩ Cube texture could be easily developed in the Ni–5W (at.%) [Ni–14W (wt%)] alloy due to its high stacking fault energy compared to other Ni–W alloys like Ni–7W or Ni–9W (at.%) [3, 4].

Conventional thermo-mechanical processing (TMP) such as rolling followed by annealing treatment allows an easy development of the {001}⟨100⟩ Cube texture [1]. However, the volume fraction of this Cube texture strongly depends on the thermo-mechanical processing (TMP) conditions [3, 5]. It was demonstrated that by increasing the thickness reduction during cold rolling of pure Ni, the stored energy increased and strengthened both the rolling

texture and the recrystallized Cube texture sharpened [5], the rolling temperature had little effect on the {001}⟨100⟩ Cube texture [5].

During the last decades, Severe Plastic Deformation (SPD) techniques, particularly accumulative roll bonding (ARB) processing, have proven their ability to produce ultra-fine grained microstructures and to accumulate very large strains without changing the initial dimensions of the original sheet [6–10]. Quite strong strain levels (equivalent strain ε > 10) could be introduced in the material via this technique while conventional rolling may lead to lower values (ε ~ 4.6 after 99% thickness reduction) due to the decreasing thickness limitation of the sheets [11].

Recently, highly textured Ni substrates were fabricated via ARB processing [11], and the deformation microstructure and texture of pure Ni after 8 ARB cycles (ε = 6.4) were compared with those of same material but cold rolled to 95% thickness reduction (ε ~ 3) [11]. It was found that ARB processing led to much more grain refinement than cold rolling, while the texture evolution was very similar [11].

In practice, one ARB cycle consists of rolling two sheets together (50% thickness reduction), cutting, wire brushing of the surface and stacking them to achieve the initial thickness [12]. Such a complex plastic deformation (combination of plane strain deformation and shear deformation) in each ARB cycle introduces significant through-thickness heterogeneities in the microstructure and texture [7, 13–18]. Usually, the mid-thickness of the ARB processed material is characterized by elongated grains along the rolling direction and exhibits a typical rolling texture, while equiaxed grains with typical shear texture are observed in the external layers [7, 10, 14, 18].

Annealing characteristics after ARB processing have been reported for many face-centered cubic (FCC) materials with high to low stacking fault energy [8, 11, 18–20]. A clear dependency of the recrystallization process on the sample scale heterogeneities was found. However, some inconsistent observations and scenarios have been reported depending on the material, deformation processing and annealing conditions. For example, the annealing texture near the mid-thickness was a retained deformation texture in pure Al [6], Al/AlSc composite [8] and pure Ni [21]. Otherwise, the shear-type texture, that was mainly of rotated cube {001}⟨110⟩ component, developed at the surface region of ARB processed pure copper was replaced by a {001}⟨100⟩ Cube texture after annealing [22].

Up to now, little studies were devoted to investigate the variation of microstructure and texture through thickness during the annealing of ARB processed Ni-based alloys [11, 16, 17, 23]. It was assumed that nearly 100% {001}⟨100⟩ Cube texture was obtained in pure Ni deformed by ARB processing and annealed at 800 °C for 1 h [11]. Results showed that the homogeneity of the texture through the

thickness was obtained after 8 ARB cycles (ε = 6.4), but the near surface and near center position was not clearly analyzed [11]. However, the recrystallization behavior along the multiscale heterogeneity of pure Ni was investigated after cold rolling [24] and only for sample processed by ARB to 6 cycles (ε = 4.8) and annealed at 200 °C for different time periods (up to 210 min) [16, 17]. It was found that the fraction of {001}⟨100⟩ Cube texture was lower in the subsurface layers than in the center and intermediate layers of the sample due to the strong shear texture [17]. In addition, the recrystallization kinetics in ARB processed Ni were strongly different from those for Ni deformed by conventional rolling [17]. It was also demonstrated that the spatial arrangement of bonding interfaces produced during ARB processing caused additional heterogeneity in the microstructure and texture [17]. It was shown that the growth of random ultrafine grains in the vicinity of bonded interfaces inhibits sharp {001}⟨100⟩ Cube texture [17]. Similar observations were reported for ARB processed Fe−36Ni and copper alloys [19, 25].

Nevertheless, the effect of ARB cycles number and the development of bonded interfaces during recrystallization and grain growth annealing treatment of Ni-based alloys have not been elucidated yet. Therefore, some through thickness morphological peculiarities and textural characteristics through of Ni−14W (wt. %) processed by ARB up to 4 cycles (ε = 3.2) and annealed at 1100 °C for 1 h are displayed in the present study. Particular attention was given on the evolution of bonded interfaces as function of ARB processing and annealing treatment.

2 Experimental procedure

The commercial Ni−14W (wt%) alloy was kindly provided by APERAM alloys society, France in the form of strips of 1 mm in thickness. The initial microstructure of the alloy was characterized by an elongated grain morphology resulting from a rolling process [26].

The strips were cut into 15×50 mm^2 rectangular pieces, degreased in acetone, and wire-brushed to remove the surface oxide film and achieve a good bonding. The strips were stacked and preheated at 450 °C for 10 min; they were then co-laminated with a two-high mill of 2.2 kW of power, rolls of 67 mm in diameter and a rotating speed of 0.14 m/s. This process was repeated up to 4 ARB cycles. The samples were then annealed at 1100 °C for 1 h under H$_2$ atmosphere. The temperature rise and cooling rates were 50 and 300 °C per hour, respectively. The annealing protocol was chosen to reproduce the real industrial conditions.

The microstructure and texture were investigated using SEM-EBSD technique in the Rolling Direction-Normal Direction (RD-ND) plane of the samples after mechanical

and electro polishing using the A2 Struers elecrolyte at 25 V. The EBSD data acquisition and analysis were undertaken using TSL Orientation Imaging Microscopy, OIM™ software.

The scanned areas, from full sample thickness in the RD-ND plan, for 1 and 2 ARB samples were of 760×1000 μm^2 and for 3 ARB sample was 1000×1000 μm^2 with a step size of 1 μm. For 4 ARB sample, the scanned area of 460×1000 μm^2 with a step size of 1 μm was measured only from the center to the surface layer of the sample.

The grain size data were estimated using a grain tolerance angle of 5° and the minimum grain size was chosen as 2 pixels. All datum points with a confidence index (CI that quantifies the reliability of the indexed pattern) lower than 0.05 were excluded from the measurements [27].

The quantitative texture analysis was carried out by calculating the Orientation Distribution Function (ODF) using MTex software [28].

3 Results and discussion

3.1 Microstructural and textural characteristics through sample thickness

Figures 1, 2, 3 and 4 present the Index Quality (IQ) and the orientation imaging micrographs (OIM) in inverse pole figure (IPF) maps showing the microstructure of the ARB processed and annealed Ni–14W alloy after 1, 2, 3 and 4 ARB cycles, respectively. The EBSD results of
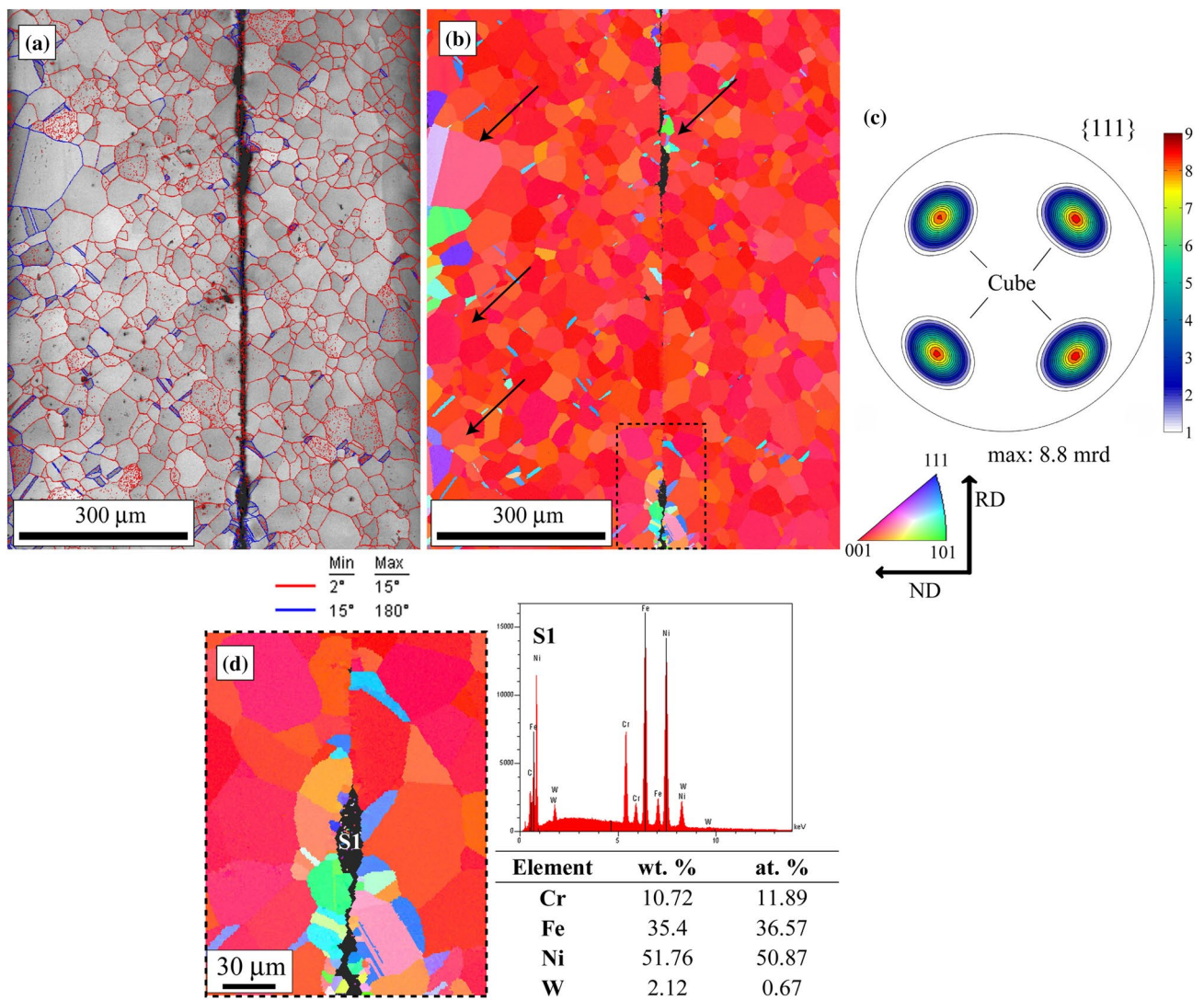

Element	wt. %	at. %
Cr	10.72	11.89
Fe	35.4	36.57
Ni	51.76	50.87
W	2.12	0.67

Fig. 1 EBSD results of Ni–W alloy after 1 ARB cycle and annealing: **a** IQ maps with LAGB (in red line) and HAGB (in blue line), **b** IPF maps, **c** recalculated {111} pole figure and **d** IPF map of selected region from **b** showing the grains with random orientation around the bonding interface and analyzed S1 point obtained by EDS

Fig. 2 EBSD results of Ni–14W alloy after 2 ARB cycle and annealing: **a** IQ maps with LAGB (in red line) and HAGB (in blue line), **b** IPF maps, **c** texture measured at the surface and interior layers in term of recalculated {111} pole figure and **d** IPF map of selected region from **b** showing the grains with random orientation around the bonding interface and analyzed S2 point obtained by EDS
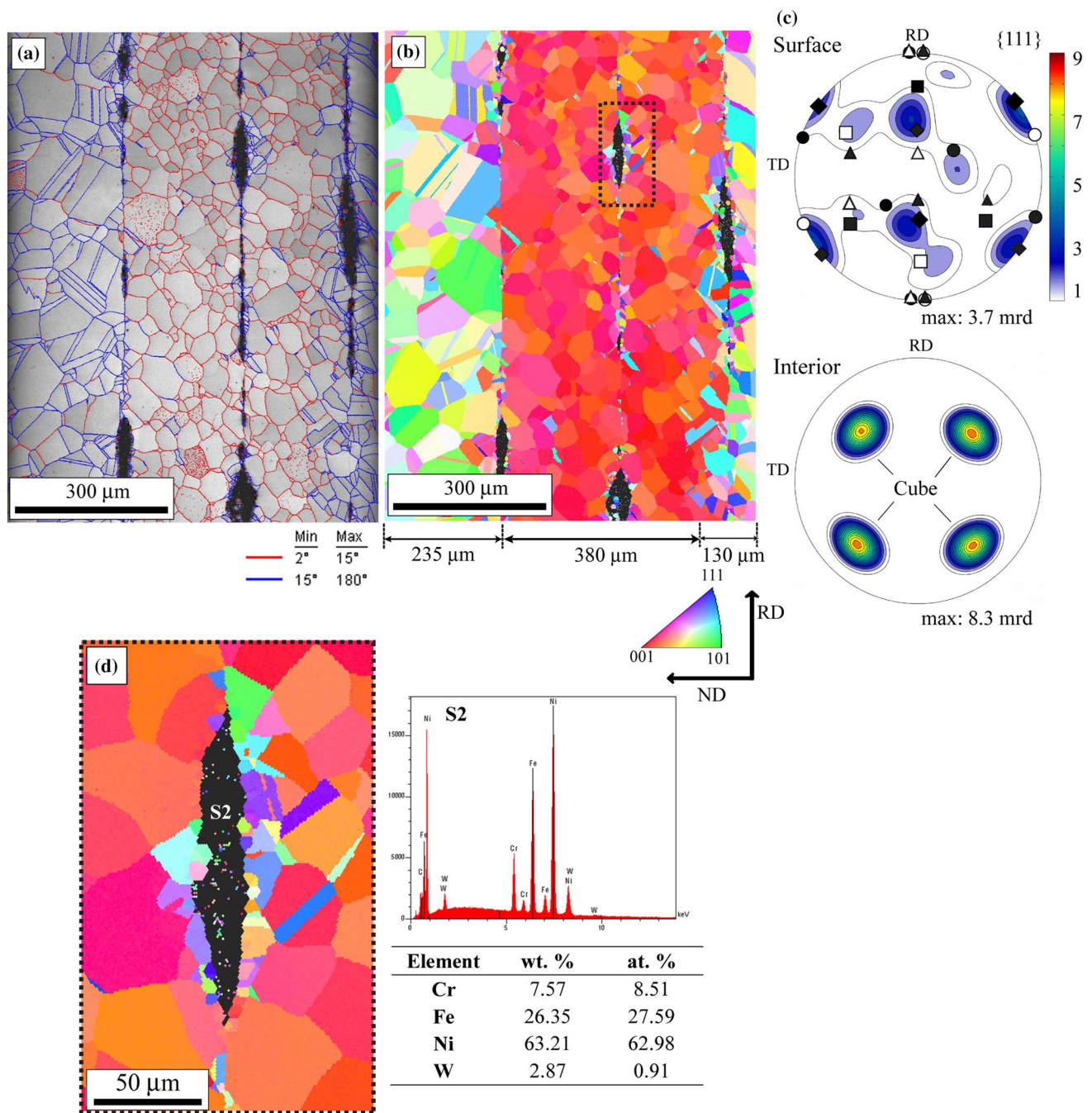
all samples are presented from one surface to the other surface covering the entire Ni–14W thickness along the normal direction (ND), except for the 4 ARB cycle sample that covers regions only from sample center to the surface layer. The red and blue lines in IQ maps represent the low angle grain boundaries (LAGBs) and the high angle grain boundaries (HAGBs), respectively. In addition, Fig. 5 shows the evolution of the grain boundary types (LAGB, twin and HAGB) and the mean grain size for the surface and interior layers as function of number of ARB cycles.

The 1 ARB cycle sample exhibits a relative homogenous microstructure characterized by high fraction of LAGBs (87%) and equiaxed grains ($d \sim 47$ μm). The evolution of the deformation microstructure of a similar Ni–14W alloy
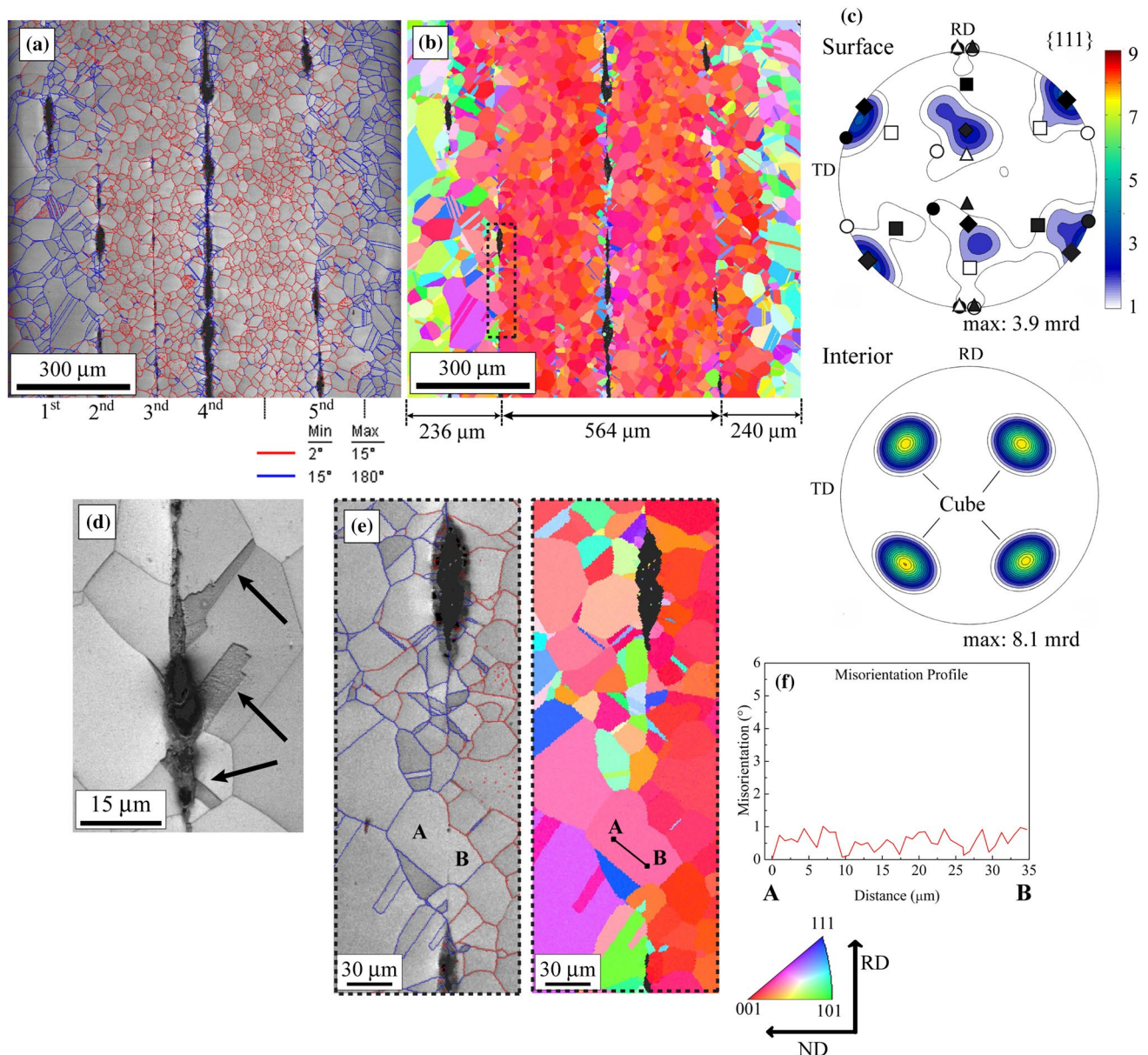
Fig. 3 EBSD results of Ni–14W alloy after 3 ARB cycle and annealing: **a** IQ maps with LAGBs (2°–15°) and HAGBs (>15°) are represented by red and blue lines, respectively, **b** IPF maps, **c** texture measured at the surface and interior layers in term of recalculated {111} pole figure, **d** IQ zone showing the formation of twins in the vicinity of interface, **e** zone showing the migration of grain boundary along the bonding interface and **f** the misorientation profile along the AB distance shown in (**f**)

(with different initial microstructure) after ARB processing has been reported in a previous work where the initial microstructure was characterized by equiaxed grains with a mean grain size of 10 μm [10]. After ARB processing, the grains gradually became flat and elongated parallel to the rolling direction and their thickness was significantly reduced to 0.2 μm after 4 ARB cycles [10]. In the present study, the fraction of LAGBs increases to 92% in the internal layers of the annealed 4 ARB cycles sample, as shown in Fig. 5a. Quite lower fraction of LAGBs (83.7%) was reported

for Ni–14W alloy after hot rolling at 1100 °C up to 50% of thickness reduction and subsequent annealing at 1000 °C for 1 h [4]. The presence of high fraction of LAGBs, even if the alloy was totally recrystallized, was attributed to the similarity of grain orientations in the interior layers. Actually, the presence of LAGBs in the epitaxial superconductor layer is fundamental to ensure high critical current density [11]. As shown in Figs. 1b, d the majority of the grains have a red color which corresponds to the Cube {001}⟨100⟩ orientation. However, some texture heterogeneity could

be detected in the 1 ARB sample such as grains having different orientations located at the surface layers and along the bonding interfaces (shown by arrows). These heterogeneities are more pronounced in samples processed to 2 ($\varepsilon = 1.6$) and 3 ($\varepsilon = 2.4$) ARB cycles. As it can clearly be seen from Figs. 2 and 3, the microstructure of surface layers of both samples is completely different from that of the internal layers. The surface thickness is in the range 130– 240 µm for both samples (2 and 3 ARB cycles). The grains are much larger and contain high fraction of twins at the surface than at the internal layers. It is well known that the evolution of recrystallized grains size during annealing is strongly related to the deformed grains and deformation history. It has been established that the grain size distribution through thickness of the Al sheet processed up to 8 ARB cycles ($\varepsilon = 6.4$) correlated well with the shear strain distributions [29], i.e. the grain size was smaller at the thickness position having higher amount of equivalent strain [29]. In addition, during each ARB cycle the surface layer with large shear deformation will move to the center layer and subsequently undergoes plane strain deformation in the next cycle. Such strain path change during ARB processing has a great impact on the grain refinement in the internal layers. As a consequence, during annealing, the recrystallized grain size in the internal layer will be smaller than those near the surface layers.

The {111} pole figures shown in Figs. 2c, 3c demonstrates that the texture at the surface layers is typical of a shear texture [30], while, the internal layers have a {001}⟨100⟩ Cube texture. The main ideal shear texture component positions of the FCC alloys are presented in the pole figures, and their descriptions are given in Table 1. As can be seen, the texture intensity at the surface layers is similar for both samples (~ 3.7 mrd, multiple random of distribution) and all shear components are developed. However, the deviation from their ideal position seems to decrease between 2 and 3 ARB cycles. The variation of the texture along the thickness of the ARB processed sheets has been already reported in the literature [7, 13]. The ARB processed alloys usually developed a texture gradient

manifested by a typical rolling texture (Copper, Brass and S components) near the mid-thickness layer and shear type texture (C and {111}//ND components) near the surface layers [7, 13, 18]. This behavior was attributed to the redundant shear strain induced by high friction between the material and the roll during the ARB processing [7, 13]. As it is well established, the annealing of rolling texture leads to the formation of {001}⟨100⟩ Cube texture [7, 18]. This evolution was thought to be caused by a mechanism of preferential growth of Cube grains that may engulf the deformed ones during the primary recrystallization process. Meanwhile, the shear texture at the surface layer seems to be retained after annealing treatment in ARB processed pure Al [18] and in ARB processed pure Ni [17]. In fact, the shear texture components are retained regardless the deformation processing or the type of recrystallization treatments [18, 31]. Based on the through thickness observations of post deformed and annealed pure Al, it was concluded that the microstructure was restored mainly by continuous static recrystallization at the surface layers and by a mixture of continuous and discontinuous static recrystallization in the interior layers [18].

Presently and in contrast, it seems that the heterogeneity level decreases with increasing number of ARB cycles. A close inspection of the surface layers of 3 ARB sample shows that it contains some Cube grains. Even if only the half thickness of 4 ARB sample is shown (Fig. 4) it can be clearly seen that the thickness of the surface layer shrinks to 95 µm and the shear texture weakens and get replaced by Cube texture (Fig. 4b). Moreover, the presence of random grains around the bonding interface seems to drastically decrease, indicating a good bonding.

It was demonstrated that the shear texture developed at the surface layers would be transformed to a rolling texture when it is transferred to the mid-thickness layers during each ARB cycle [7, 32]. Previously, it has been demonstrated by Visco-Plastic Self-Consistent (VPSC) simulation that all shear (A_1^*, A, B and C) components are transformed to rolling texture components (Copper, Brass, S) under plane strain compression (PSC) deformation during 1 ARB cycle [33]. Moreover, it was observed that the shear texture intensity at the surface layers decreases drastically with the increasing number of ARB [7] and cross ARB cycles [33], indicating that the shear-type textures at the surface might not strengthen continuously with the increasing number of ARB cycles or accumulated strain [33].

Furthermore, annealing twins are evidenced in many recrystallized grains mainly near the surface layers of the sheets while they are almost absent in the internal ones. Figure 5a shows that their fraction decreases from 13 to 4% with increasing number of ARB cycles in the internal layers. Similar decrease was reported with increasing the rolling reduction ratio [5], most probably because

Table 1 Typical shear components for FCC materials

Notation		Euler angles (°)		
		φ1	φ	φ2
●	A_1^*	125	90	45
○	A_2^*	54	90	45
△	A	0	35.26	45
▲	$\overline{A}$	180	35.26	45
□	B	0	54.74	45
■	$\overline{B}$	60	54.74	45
◆	C	0	90	45

Fig. 4 EBSD results of Ni–14W alloy after 4 ARB cycles and annealing: **a** IQ maps with LAGB (in red line) and HAGB (in blue line), **b** IPF maps, **c** texture measured at the surface and interior layers in term of recalculated {111} pole figure and **d** IPF map of selected region from **b** showing the grains having sizes of layer zone and **e** zone showing the migration of grain boundary, twin and small grains along the bonding interface
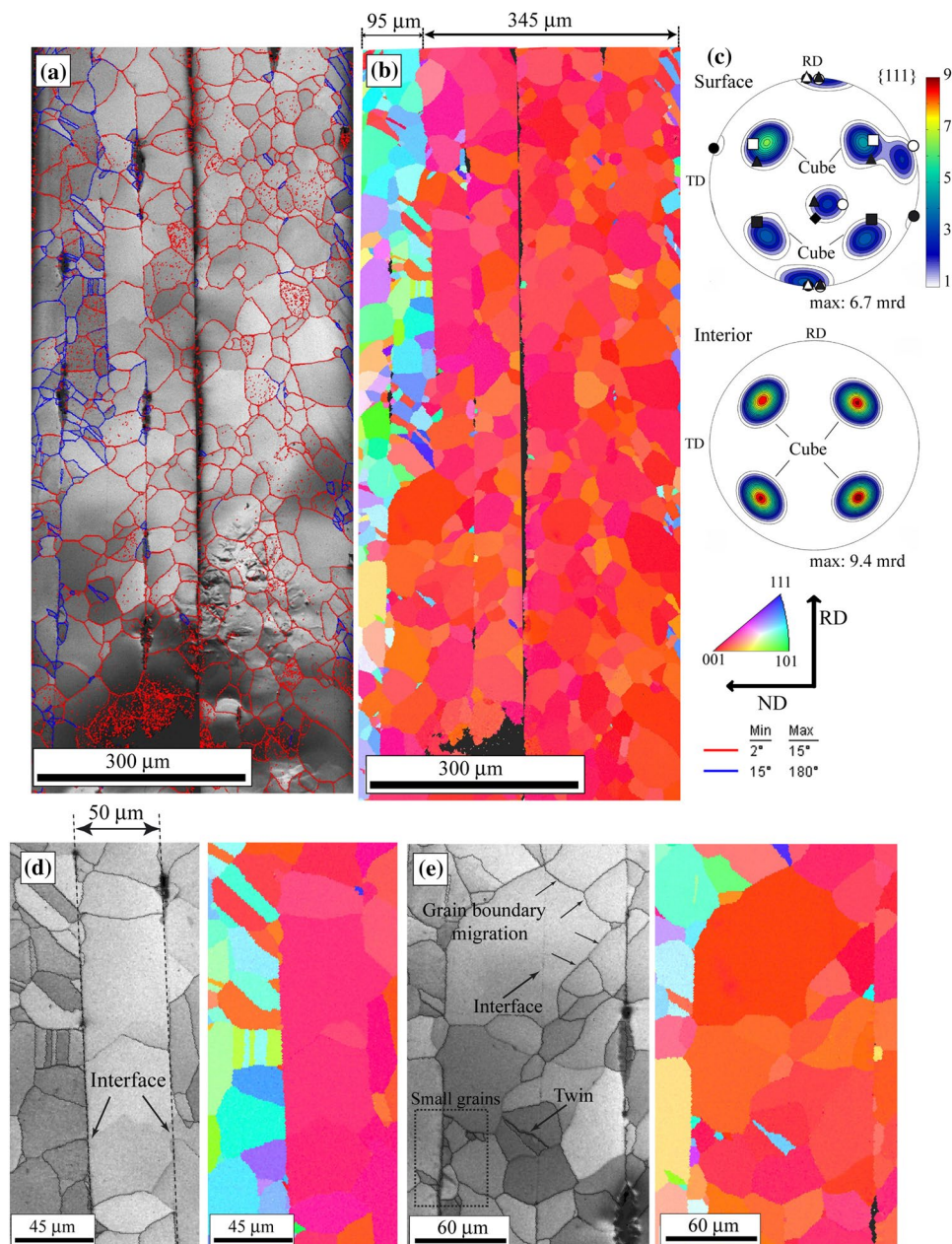
of the decreasing grain size. Moreover, it was demonstrated that the fraction of twin decreases drastically with the increasing annealing temperature from 700 to 1000 °C for hot rolled Ni–14Ni alloys [4]. The presence of twin is related to the occurrence of the recrystallization and the grain growth phenomena [34]. In fact, the strain induced boundary migration (SIBM) mechanism is responsible for the recrystallization and twinning in rolled Ni-based alloys [34]. In this mechanism, the orientations of the recrystallized grains are similar to those of the deformed one [35], which is in good agreement with the evolution of the texture at the surface layers as shown in Figs. 2 and 3.

In addition, twin formation during annealing of Ni-based alloys was considered as an "accident" during grain boundary migration [34]. The suppression of annealing twins was supposed to be benefic to increase the intra/inter-granular current transport in the epitaxial superconductor layer [11]. Moreover, Fig. 5a clearly shows that the presence of high fraction of twins at the surface region is associated with the presence of high fraction of HAGBs. In addition, the fraction of HAGBs and twins are very close. The twin fraction at the surface region increases rapidly form 7% after 1 ARB cycle to 42% after annealing of the 2 ARB cycles sample and continuously decreases after 3 ARB cycles (37%) and reaches a fraction of 7% for 4 ARB sample.

Fig. 5 Evolution of **a** fraction of LAGBs, twins and HAGBs and **b** mean grain size in surface and interior layer of Ni–14W alloy after ARB processing and annealing
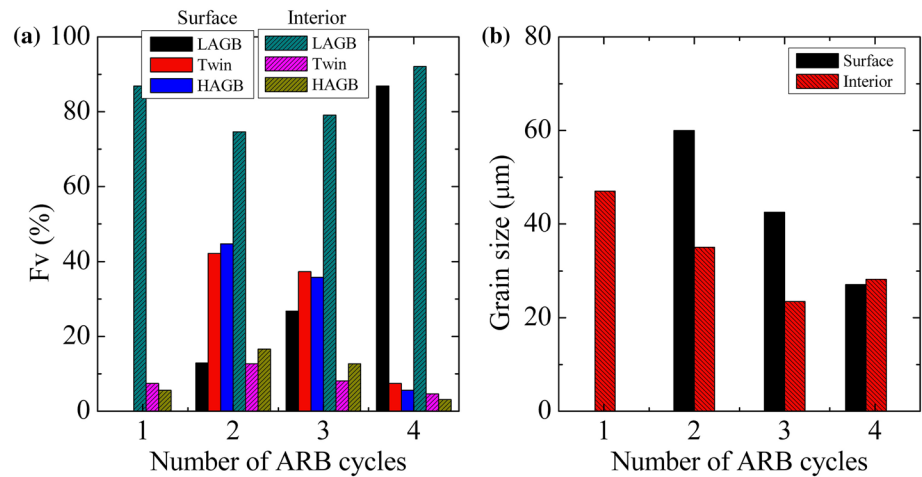

Figure 5b shows the evolution of the mean grain size, without considering twins, at the surface and internal layers after ARB processing and annealing. As expected, the grain size decreases with the increasing ARB cycle number in both types of layers. Obviously, the grain size at the surface layers is higher than at the internal ones. In contrast, it was observed that the grain size near the center was slightly larger than that of the surface in cold rolled and annealed pure Ni [24]. These contradictory results are explained based on the nature of the deformation processing. Unlike the conventional rolling, during the next ARB cycle the surface layer will be transformed to interior layer due to the sheet cutting step. Basically, the stored energy in the interior layers will be always higher than that at the surface layers.

As shown in IQ maps and Fig. 5b, the grains at the surface layers are bonded by HAGBs which causes a further growth due the mobility of HAGBs compared to the LAGBs [36]. Experimental and simulation works evidenced a variable motion of the interfacial boundaries between the layers; the "oldest" bonded interfaces having higher mobility than the new ones [37]. Then, it was concluded that the last ARB cycle leads to an additional obstacle for grain boundary migration at the central interface [37]. Consequently, the mean grain size in the new layer is smaller than in the older ones leading to through thickness anisotropic distribution.

The grain size of the present alloy is significantly higher [28 μm after 4 ARB cycles ($\varepsilon = 3.2$)] than that reported for ARB processed pure Ni and annealed at 300 °C for 1 h [14 μm after 5 ARB cycles ($\varepsilon = 4$)] [23]. The difference may be attributed to the higher annealing temperature used in the present study (1100 °C) which obviously causes grain growth. In fact, it was reported that the microstructure of the annealed ARB processed pure Ni ($\varepsilon = 6.4$) at 300 °C for 15 s contain already 15% of recrystallized grains [11]. The rapid recrystallization and increase of the grain size may be

explained by the high sorted energy accumulated during the ARB processing [23].

3.2 Microstructural and textural characteristics at the bonded interface

Quite interesting features can be observed along the bonded interfaces in all annealed samples. Figures 1d and 2d show the presence of small cluster of grains with random orientation along the bonded interfaces. The nucleation and growth of such random small grains along the bonded interface has been already reported in ARB processed and annealed pure Ni [17], Fe–36Ni (wt%) alloy [19] and pure Copper [20]. Two main reasons were proposed to explain their occurrence: (i) the existence of large shear strain induced at the sheet surfaces due to the friction between the rolls and material and (ii) the effect of wire-brushing and stacking process during the sample preparation [19, 20]. Actually, the IPF map of 1 ARB sample (Fig. 1b) shows very small fraction of shear grains at the edge of the sample. In contrast, Fig. 1d shows that the random oriented small grains have already developed soon after 1 ARB cycle which indicates that wire-brushing is the main responsible mechanism. Energy dispersive spectroscopy (EDS) analysis of point S1 (Fig. 1d) and point S2 (Fig. 2d) in black zone along the bonded interface obviously show the presence of high fraction of iron (Fe) and chromium (Cr) elements. The presence of these particles (like S1, S2) originated from the fragments of the steel wire brush used during surface preparation. Similar observation was reported in ARB processed Ni alloy [16]. The presence of these steel particles allows the formation of new recrystallized grains with random orientation, which is ascribed to particle stimulated nucleation (PSN) mechanism [31]. It is interesting to note that their grain size decreases with the increasing number of ARB processing (Figs. 1, 2, 3).

Figure 3d shows also that several twins preferably generated on interfacial grains in the bonded interface containing particles (black zone). Similar observation was reported in ARB processed and annealed Copper [38]. The generation of twins in the interfacial grains was also found on Ni and Cu alloys produced by hot compressive bonding (HCB) [39, 40].

It was found that the number of steel particles increased with increasing number of ARB cycles up to 6 cycles [16]. Meanwhile, in the present study, the bonded interfaces containing the steel particles seem to decrease (almost disappeared) after 4 ARB cycles (Fig. 4). This observation is in good agreement with the assumption that PSN mechanism may occur at low rather than at high strain deformation [31, 41, 42]. Moreover, the number of "visible" bonded interfaces decreased for 3 and 4 ARB cycles samples. For example, 3 ARB cycles sample is supposed to contain 7 bonded interfaces ($2^N − 1$), where N is number of ARB cycles. While, in Fig. 3 it is possible to detect only 5 bonded interfaces may possibly be detected, the 2 missing interfaces disappeared and were replaced by recrystallized grains and curved grain boundaries crossing all over the layer thickness. This result shows clearly that a good bonding is achieved and more homogenous microstructure could be obtained with increasing number of ARB cycles. The increase of interfaces fraction crossed by the grain boundaries with increasing number of ARB cycles was observed experimentally and theoretically using the two dimensional Potts model for high purity Al [43].

Interesting features can be observed in Figs. 3e and 4e where grains cross through the bonded interface. The interfacial grain boundary migrates and leaves a "ghost" line at the original position of the bonded interfaces. As can be seen from Fig. 3f, any strong misorientation between A and B points could be highlighted across the bonded interface and this indicates that A and B points belong to the same grain.

It has been stated that the grain boundaries got more curved after migration [44]. By contrast, Fig. 4d shows that some interfacial boundaries are straight and perfectly parallel to the rolling plane. It is worth noting that the orientations of grains located on each side of this bonded interface are different. The grain sizes in this layer have almost the same thickness than that of the layer (~ 50 μm) and no crossing grain boundary is detected in this layer. In this case, the bonded interfaces act as barriers against grain growth.

It is reasonable to consider that the texture difference, from one side of the layer to the other is the main cause of the non-curvature and the low mobility of the interfacial grain boundary. Basically, the grain boundary properties are strongly related to the texture since the grain
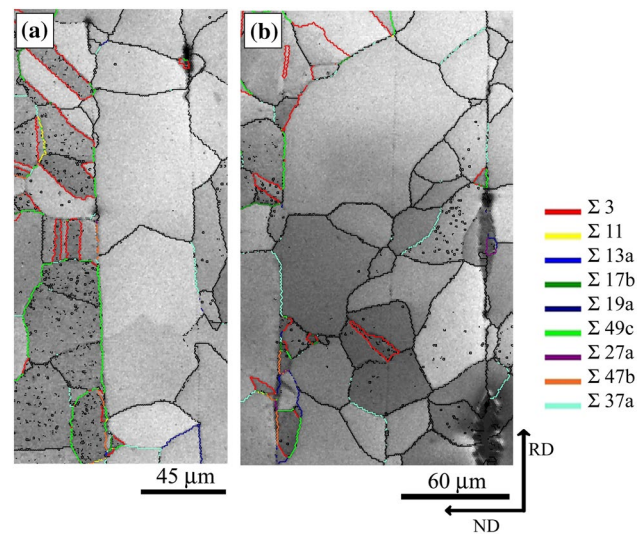

Fig. 6 **a**, **b** IQ maps superposed with different CSL boundaries from particular zones along the bonded interfaces of Ni–14W alloy after 4 ARB cycles and annealing

boundary misorientation arises from the crystallographic orientation relationships between neighboring grains [45].

Another feature can be noticed in Fig. 4e where the grain size is not uniform along the interfacial grain boundary. Some grains are visibly large due the high migration of their grain boundaries and others are very small (as shown in the box in the Fig. 4e) because of the low migration rate of their grain boundaries.

These observations about the recrystallized grains along the bonded interfaces are strongly related to their migrating grain boundaries. In fact, several factors can be responsible for these features. Among them, firstly, the migration of grain boundaries after annealing treatment may depend strongly on the stored energy of the specific grain during the deformation processing. Indeed, it was observed that, during compression bonding at high temperature (ranging 1000–1150 °C) of Ni-based alloy, the grain boundaries migrated from one side of the interface, having low dislocation density, to the other side with high dislocation density [39]. The stored energy rate is known to be related to the orientation of the grain during the deformation processing [46]. The crystallographic orientation of grains and their neighborhood are the main responsible for the mobility of their grain boundaries. Secondly, a good correlation between grain boundary geometry and their mobility has been well established [47, 48]. Indeed, the grain boundaries with high-angle special boundaries with some ordered structure such as coincidence-site lattice (CSL/Σ) boundaries are known to be inactive (immobile) during solid state transformation evolving from the grain boundaries like discontinuous precipitation or ordering

Table 2 Special misorientation of CSL grains boundaries and their angle/axis representation found in IQ maps of 4 ARB sample (shown in Fig. 6)

CSL boundary	θ° ⟨hkl⟩
Σ3	60° ⟨111⟩
Σ 11	50.48° ⟨110⟩
Σ 13a	22.62° ⟨100⟩
Σ 17b	61.93° ⟨221⟩
Σ 19a	26.53° ⟨110⟩
Σ 27a	31.58° ⟨110⟩
Σ 37a	18.92° ⟨111⟩
Σ 47b	43.66° ⟨320⟩
Σ 49c	49.22° ⟨322⟩

Table 3 Fraction of CSL boundaries as function of number of ARB cycles

	1 ARB	2 ARB	3 ARB	4 ARB
CSL (%)	8.2	31.5	22.8	10

reactions [47, 48]. Figure 6 clearly revealed that the straight interfacial grain boundaries and the small grains are surrounded by CSL boundaries. Table 2 presents the angle and axis of misorientation for the CSL boundaries. It is believed that the CSL boundaries have lower energies than general or random grain boundaries (black line) [49]. This explains why grains surrounded by CSL boundaries remain small in respect to the low boundary mobility that may hinder the grain growth during annealing. Contrarily, grains with random grain boundary develop more easily.

It has been demonstrated that grain refinement obtained by thermo-mechanical processing promotes the

formation of CSL boundaries i.e. the fraction of Σ boundaries (Σ1—Σ29) increases with decreasing grain size [50]. However, Table 3 shows that the fraction of CSL boundaries increases considerably after annealing of the 2 ARB cycles sample (31.5%) and decreases with the increasing number of ARB cycles (22.8% for 3 ARB cycles sample and 10% for 3 ARB cycles sample).The considerable decrease of CSL boundaries after 4 ARB cycle can be related to their poor statistics since only half sample thickness was analyzed for this sample. It may be recognized that the fraction of CSL boundaries decreases with decreasing the texture heterogeneity through samples thickness.

3.3 General texture evolution

Figure 7 illustrates the evolution of annealing texture in terms of ODF sections at $\varphi_2 = 0$, 45 and 65° of the Ni–14W alloy as a function of the number of ARB cycles. It is obvious that the texture is recrystallization-type with a net predominance of Cube {001}⟨100⟩ component. It is worth noting that the deformation texture after ARB processing in similar Ni–14W alloys was characterized by a Copper-type where the Copper {112}⟨111⟩, S {132}⟨643⟩ and Brass {110}⟨112⟩ were the principal texture components [10]. As can be seen from Fig. 7, the Cube texture drastically weakens after the first ARB cycle (intensity from 42 to 19 mrd). This decrease was attributed to the presence of shear texture at the sample surface as shown in Fig. 2 and 3.

It is interesting to analyze the sharpness of Cube texture in the annealed ARB sample in terms of deviation from ideal position, because of the epitaxial microstructure control and even for the easy ⟨100⟩ magnetization directions
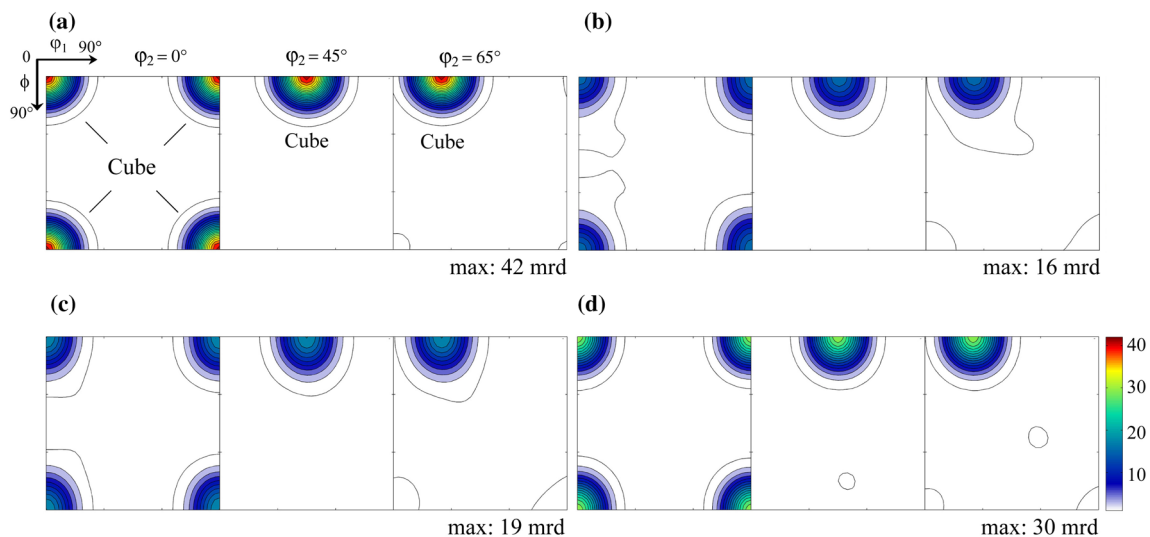

Fig. 7 ODF sections at $\varphi_2 = 0$, 45 and 65° of Ni–14W alloy after ARB processing and annealing at 1000 °C for 1 h: **a** 1, **b** 2, **c** 3 and **d** 4 ARB cycles

as stated in [51]. Figure 8 shows the OIM maps of only Cube oriented grains with different shades depending on their deviation from the ideal Cube position (0°,0°,0°) while Fig. 9 presents the volume fraction of Cube orientation with deviation smaller than 5°, in the range of 5°–10° and 10°–15° as a function of the number of ARB cycles. The analysis of these two figures point out that the majority of the Cube grains have a deviation between 5°–10°. Only 1 ARB sample exhibits high fraction of Cube grains with less than 5° (35%) and it seems that these Cube grains with less than 5° are located along the entire thickness of the sample at low number of ARB cycle ($\varepsilon = 0.8$) and more located at the interfaces and near to the surfaces layers at higher number of ARB cycles ($\varepsilon = 2.4$–3.2).

Finally, the results of the present study demonstrate the existence of microstructural and textural inhomogeneities in a Ni–14W sheet processed by ARB up to 4 cycles ($\varepsilon = 3.2$) and annealed at 1100 °C for 1 h. These inhomogeneities do evolve upon the increasing strain. Achieving

Fig. 9 Evolution of the fraction Cube component at different deviation from the ideal Cube position (0°, 0°, 0°)

homogeneous microstructure and sharp Cube texture in coated conductor substrates for photovoltaic devices is tremendously important. It should be necessary, to ensure a better microstructural and textural homogeneity, to deeply analyze the mechanism of their formation. The through-thickness microstructure and texture difference, as well as the nucleation and growth of small-sized grains probably due to the injection of steel particles during wire brushing, should arouse a convinced interest. Preliminary EDS results show that these particles do not seem to be pure steel but maybe a kind of complicated solid solution containing Ni and W that formed during the hot ARB processing. The complicated role of special boundaries is also a stimulating task.

4 Conclusion

The Ni–14W alloy was processed by ARB to 1, 2, 3 and 4 cycles and subsequently annealed at 1100 °C for 1 h. The EBSD analyses reveal a net through thickness heterogeneity of the 4 samples:

- For the internal layers, the microstructure exhibits a small grains size, free of twins, and contains high fraction of low angle grain boundaries due the domination of the Cube {001} ⟨100⟩ orientation.
- For the surface layers, the grains are larger and contain a high fraction of twins, while the texture is characterized by retained shear texture components.

At bonded interfaces, the new recrystallized grains are smaller and randomly orientated due to the presence
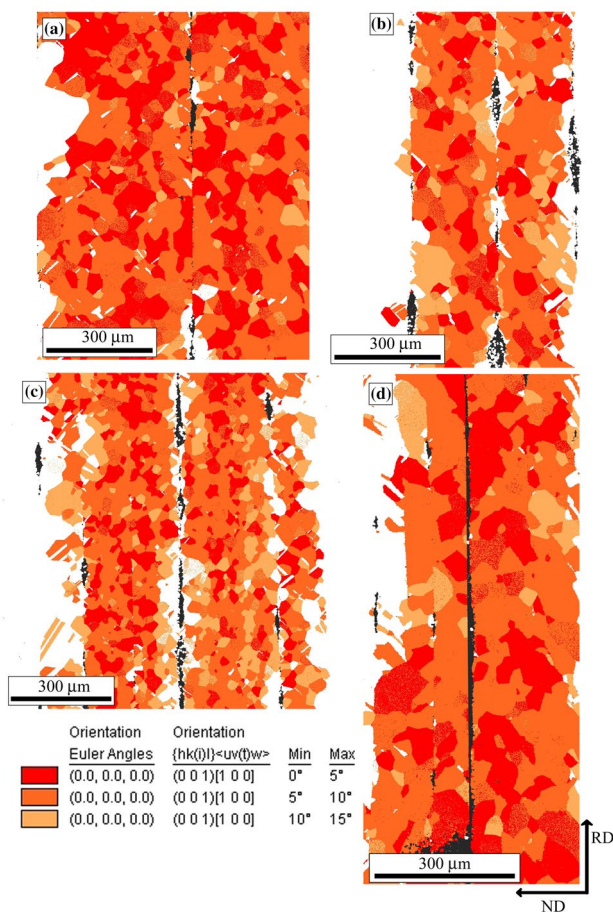

Fig. 8 OIM maps of the processed and annealed Ni–14W alloy showing the Cube fraction at different deviation from the ideal Cube position (0°,0°,0°): **a** 1 ARB, **b** 2 ARB, **c** 3 ARB and **d** 4 ARB cycles
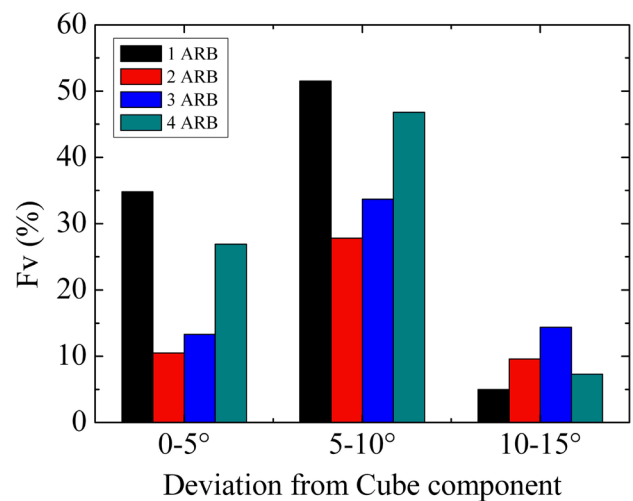
of particles resulting from the wire-brushing procedure. It was shown that these heterogeneities are strongly dependent on the number of ARB cycles:

- The microstructure and texture heterogeneities decrease with the increasing number of ARB processing.
- The bonded interfaces were eliminated with the increasing number of ARB cycles and transformed themselves to migrated interfacial grain boundaries synonymous of successful bonding.
- The recrystallized grain size along the bonded interfaces was related to the grain boundary network. Small grains are shown to be surrounded by inactive special CSL boundaries, while large grains with random grain boundaries which promoted their migration.

Data availability The raw/processed data required to reproduce these findings cannot be shared at this time as the data also forms part of an ongoing study.

Compliance with ethical standards

Conflict of interest The authors declare that they have no conflict of interest.

References

1. Bhattacharjee PP, Ray RK, Upadhyaya A (2007) Nickel base substrate tapes for coated superconductor applications. J Mater Sci 42(6):1984–2001. https://doi.org/10.1007/s10853-006-1416-6
2. Borisov AV, Rakov DN, Abdyukhanov IM, Potapenko MM, Mikhalev AV, Gryaznov NS, Klinevskii MG (2016) Composite textured substrate tape for second-generation high-temperature superconductors with low magnetic susceptibility. At Energ 119(5):326–331. https://doi.org/10.1007/s10512-016-0067-1
3. Sarma VS, Eickemeyer J, Mickel C, Schultz L, Holzapfel B (2004) On the cold rolling textures in some fcc Ni–W alloys. Mater Sci Eng A 380(1):30–33. https://doi.org/10.1016/j.msea.2004.05.024
4. Gao M, Zhang F, Liang S, Li H, Ma L, Liu M, Kausar S, Suo H (2019) Influence of cube texture development on magnetic properties of Ni–5 at.%W alloy substrates. J Magn Magn Mater 469:515–521. https://doi.org/10.1016/j.jmmm.2018.09.029
5. Chang H, Baker I (2007) Effects of degree of deformation and deformation temperature on primary recrystallization textures in polycrystalline nickel. Metall Mater Trans A 38(11):2815–2824. https://doi.org/10.1007/s11661-007-9324-1
6. Kamikawa N, Huang X, Tsuji N, Hansen N (2009) Strengthening mechanisms in nanostructured high-purity aluminium deformed to high strain and annealed. Acta Mater 57(14):4198–4208. https://doi.org/10.1016/j.actamat.2009.05.017
7. Tirsatine K, Azzeddine H, Baudin T, Helbert A-L, Brisset F, Alili B, Bradai D (2014) Texture and microstructure evolution of Fe–Ni alloy after accumulative roll bonding. J Alloy Compd 610:352–360. https://doi.org/10.1016/j.jallcom.2014.04.173
8. Quadir MZ, Najafzadeh N, Munroe PR (2016) Variations in through-thickness recrystallization and grain growth textures in the Al layers in ARB-processed Al/Al(0.3% Sc) composite sheets. Mater Des 93:467–473. https://doi.org/10.1016/j.matdes.2015.12.106
9. Tirsatine K, Azzeddine H, Baudin T, Helbert AL, Brisset F, Bradai D (2017) Microstructure and microtexture evolution of invar alloy after cross accumulative roll bonding (CARB) compared to ARB. Mater Sci Forum 879:744–749. https://doi.org/10.4028/www.scientific.net/MSF.879.744
10. Boudekhani S, Azzeddine H, Tirsatine K, Baudin T, Helbert A-L, Brisset F, Alili B, Bradai D (2018) Microstructure, texture, and mechanical properties of Ni–W alloy after accumulative roll bonding. J Mater Eng Perform 27(10):5561–5570. https://doi.org/10.1007/s11665-018-3628-8
11. Bhattacharjee PP, Tsuji N (2011) Development of highly cube textured nickel superconductor substrate tapes by accumulative roll bonding (ARB). Int J Mater Res 102(2):173–182. https://doi.org/10.3139/146.110465
12. Saito Y, Utsunomiya H, Tsuji N, Sakai T (1999) Novel ultra-high straining process for bulk materials—development of the accumulative roll-bonding (ARB) process. Acta Mater 47(2):579–583. https://doi.org/10.1016/S1359-6454(98)00365-6
13. Kamikawa N, Tsuji N, Minamino Y (2004) Microstructure and texture through thickness of ultralow carbon IF steel sheet severely deformed by accumulative roll-bonding. Sci Technol Adv Mater 5(1–2):163–172. https://doi.org/10.1016/j.stam.2003.10.018
14. Zhang YB, Mishin OV, Godfrey A (2014) Analysis of through-thickness heterogeneities of microstructure and texture in nickel after accumulative roll bonding. J Mater Sci 49(1):287–293. https://doi.org/10.1007/s10853-013-7703-0
15. Najafzadeh N, Quadir MZ, Munroe P (2015) Through thickness microstructural and texture inhomogeneity within Al layers in ARB-produced Al-Al(Sc) layered composite sheets. Metal Mater Trans A 46(10):4772–4782. https://doi.org/10.1007/s11661-015-3056-4
16. Mishin OV, Zhang YB, Godfrey A (2017) The influence of multiscale heterogeneity on recrystallization in nickel processed by accumulative roll bonding. J Mater Sci 52(5):2730–2745. https://doi.org/10.1007/s10853-016-0566-4
17. Mishin OV, Zhang YB, Godfrey A (2017) Recrystallization texture in nickel heavily deformed by accumulative roll bonding. IOP Conf Ser Mater Sci Eng 219:012034. https://doi.org/10.1088/1757-899x/219/1/012034
18. Li S, Yang L, Qin N (2018) Development of through-thickness texture gradient and persistence of shear-type textures during annealing of commercial purity aluminium sheet processed by accumulative roll-bonding. J Mater Sci Technol 34(5):821–831. https://doi.org/10.1016/j.jmst.2017.04.019
19. Tirsatine K, Azzeddine H, Baudin T, Helbert A-L, Brisset F, Bradai D (2017) On the recrystallization and texture of Fe-36%Ni alloy after accumulative roll bonding and annealing at 600 °C. Mater Eng 24:56–66
20. Takata N, Yamada K, Ikeda K-i, Yoshida F, Nakashima H, Tsuji N (2007) Change in microstructure and texture during annealing of pure copper heavily deformed by accumulative roll bonding. Mater Trans 48(8):2043–2048. https://doi.org/10.2320/matertrans.MA200701
21. Bhattacharjee PP, Tsuji N, Ray RK (2011) Effect of initial grain size on the evolution of {001}%3c100%3e texture in severely

deformed and annealed high-purity nickel. Metall Mater Trans A 42(9):2769–2780. https://doi.org/10.1007/s11661-011-0674-3

22. Shaarbaf M, Toroghinejad MR (2009) Evaluation of texture and grain size of nanograined copper produced by the accumulative roll bonding process. Metall Mater Trans A 40(7):1693–1700. https://doi.org/10.1007/s11661-009-9851-z

23. Zhang YB, Mishin OV (2017) Stored energy and recrystallized microstructures in nickel processed by accumulative roll bonding to different strains. Mater Charact 129:323–328. https://doi.org/10.1016/j.matchar.2017.05.024

24. Jahani N, Reihanian M, Gheisari K (2019) Kinetics of recrystallization and microstructure distribution during isothermal annealing of cold rolled nickel. Mater Res Express 6(9):096504. https://doi.org/10.1088/2053-1591/ab2b29

25. Takata N, Yamada K, Ikeda K, Yoshida F, Nakashima H, Tsuji N (2006) Annealing behavior and recrystallized texture in ARB processed copper. Mater Sci Forum 503–504:919–924. https://doi.org/10.4028/www.scientific.net/MSF.503-504.919

26. Koriche S, Boudekhani-Abbas S, Azzeddine H, Abib K, Helbert A-L, Brisset F, Baudin T, Bradai D (2018) On the groove pressing of Ni–W alloy: microstructure, texture and mechanical properties evolution. Kov Mater 56:313–323. https://doi.org/10.4149/km_2018_5_313

27. Mikami Y, Oda K, Kamaya M, Mochizuki M (2015) Effect of reference point selection on microscopic stress measurement using EBSD. Mater Sci Eng, A 647:256–264. https://doi.org/10.1016/j.msea.2015.09.004

28. Bachmann F, Hielscher R, Schaeben H (2010) Texture analysis with MTEX: free and open source software toolbox. Solid State Phenom 160:63–68. https://doi.org/10.4028/www.scientific.net/SSP.160.63

29. Lee SH, Saito Y, Tsuji N, Utsunomiya H, Sakai T (2002) Role of shear strain in ultragrain refinement by accumulative roll-bonding (ARB) process. Scr Mater 46(4):281–285. https://doi.org/10.1016/S1359-6462(01)01239-8

30. Beyerlein IJ, Tóth LS (2009) Texture evolution in equal-channel angular extrusion. Prog Mater Sci 54(4):427–510. https://doi.org/10.1016/j.pmatsci.2009.01.001

31. Abib K, Azzeddine H, Tirsatine K, Baudin T, Helbert A-L, Brisset F, Alili B, Bradai D (2016) Thermal stability of Cu–Cr–Zr alloy processed by equal-channel angular pressing. Mater Charact 118:527–534. https://doi.org/10.1016/j.matchar.2016.07.006

32. Heason CP, Prangnell PB (2002) Texture evolution and grain refinement in Al deformed to ultra-high strains by accumulative roll bonding (ARB). Mater Sci Forum 408–412:733–738. https://doi.org/10.4028/www.scientific.net/MSF.408-412.733

33. Azzeddine H, Tirsatine K, Baudin T, Helbert A-L, Brisset F, Bradai D (2014) Texture evolution of an Fe–Ni alloy sheet produced by cross accumulative roll bonding. Mater Charact 97:140–149. https://doi.org/10.1016/j.matchar.2014.09.009

34. Wang W, Brisset F, Helbert AL, Solas D, Drouelle I, Mathon MH, Baudin T (2014) Influence of stored energy on twin formation during primary recrystallization. Mater Sci Eng A 589:112–118. https://doi.org/10.1016/j.msea.2013.09.071

35. Humphreys J, Rohrer GS, Rollett A (2017) Chapter 7: recrystallization of single-phase alloys. In: Humphreys J, Rohrer GS, Rollett A (eds) Recrystallization and related annealing phenomena, 3rd edn. Elsevier, Oxford, pp 245–304. https://doi.org/10.1016/B978-0-08-098235-9.00007-0

36. Bhattacharjee PP, Ray RK, Tsuji N (2009) Cold rolling and recrystallization textures of a Ni–5at.% W alloy. Acta Mater 57(7):2166–2179. https://doi.org/10.1016/j.actamat.2009.01.015

37. Lienshöft L, Chekhonin P, Zöllner D, Scharnweber J, Marr T, Krauter T, Hoeppel HW, Skrotzki W (2017) Static recrystallization and grain growth of accumulative roll bonded aluminum laminates. J Mater Res 32(24):4503–4513. https://doi.org/10.1557/jmr.2017.386

38. Suresh KS, Rollett AD, Suwas S (2013) Evolution of microstructure and texture during deformation and recrystallization of heavily rolled Cu–Cu multilayer. Metall Mater Trans A 44(8):3866–3881. https://doi.org/10.1007/s11661-013-1749-0

39. Zhang JY, Sun MY, Xu B, Li DZ (2018) Interfacial microstructural evolution and metallurgical bonding mechanisms for IN718 superalloy joint produced by hot compressive bonding. Metall Mater Trans B 49(5):2152–2162. https://doi.org/10.1007/s11663-018-1313-9

40. Zhang JY, Sun MY, Xu B, Hu X, Liu S, Xie BJ, Li DZ (2019) Evolution of the interfacial microstructure during the plastic deformation bonding of copper. Mater Sci Eng A 746:1–10. https://doi.org/10.1016/j.msea.2018.12.119

41. Oscarsson A, Ekström HE, Hutchinson WB (1993) Transition from discontinuous to continuous recrystallization in strip-cast aluminium alloys. Mater Sci Forum 113–115:177–182. https://doi.org/10.4028/www.scientific.net/MSF.113-115.177

42. Prangnell PB, Bowen JR, Berta M, Apps PJ, Bate PS (2004) Stability of ultra-fine 'grain structures' produced by severe deformation. Mater Sci Forum 467–470:1261–1270. https://doi.org/10.4028/www.scientific.net/MSF.467-470.1261

43. Chekhonin P, Zöllner D, Zimmer E, Scharnweber J, Romberg J, Skrotzki W (2019) Microstructure of accumulative roll bonded high purity aluminium laminates. Materialia 5:100236. https://doi.org/10.1016/j.mtla.2019.100236

44. Yin W, Wang W, Fang X, Qin C, Xing X (2015) Migration of grain boundaries and triple junctions in high-purity aluminum during annealing after slight cold rolling. Mater Charact 107:134–138. https://doi.org/10.1016/j.matchar.2015.07.005

45. Randle V (1993) The measurement of grain boundary geometry. CRC Press, Boca Raton

46. Azzeddine H, Tirsatine K, Baudin T, Mathon M-H, Helbert A-L, Brisset F, Bradai D (2017) On the stored energy evolution after accumulative roll-bonding of invar alloy. Mater Chem Phys 201:408–415. https://doi.org/10.1016/j.matchemphys.2017.08.063

47. Semenov V, Rabkin E, Bischoff E, Gust W (1998) The effect of the grain boundary misorientation on the kinetics of the discontinuous ordering reaction in Fe-50 at.%Co. Acta Mater 46(7):2289–2298. https://doi.org/10.1016/S1359-6454(98)80009-8

48. Azzeddine H, Abdessameud S, Alili B, Boumerzoug Z, Bradai D (2011) Effect of grain boundary misorientation on discontinuous precipitation in an AZ91 alloy. Bull Mater Sci 34(7):1471–1476. https://doi.org/10.1007/s12034-011-0345-4

49. Palumbo G, Aust KT, Lehockey EM, Erb U, Lin P (1998) on a more restrictive geometric criterion for "special" CSL grain boundaries. Scr Mater 38(11):1685–1690. https://doi.org/10.1016/S1359-6462(98)00077-3

50. Castro RSd, Ferreira RAS, Pedrosa IRV, Yadava YP (2013) Effects of thermomechanical treatment on the occurrence of coincident site lattice boundaries in high strength low alloy steel. Mater Res 16:1350–1354

51. Hutchinson B (2012) The cube texture revisited. Mater Sci Forum 702–703:3–10. https://doi.org/10.4028/www.scientific.net/MSF.702-703.3